UC Irvine

Title

The structure and effect of suture zones in the Larsen C Ice Shelf, Antarctica

Permalink

https://escholarship.org/uc/item/4158p0f9

Journal

Journal of Geophysical Research Earth Surface, 119(3)

ISSN

2169-9003

Authors

McGrath, Daniel
Steffen, Konrad
Holland, Paul R
et al.

Publication Date

2014-03-01

DOI

10.1002/2013jf002935

Copyright Information

Peer reviewed

RESEARCH ARTICLE

Key Points:
- Material heterogeneity in suture zones limit fracture propagation
- Heterogeneity is limited to lower 40% of ice thickness near calving front
- Loss of this heterogeneity will weaken ice shelf

Correspondence to:
D. McGrath,
daniel.mcgrath@colorado.edu

The structure and effect of suture zones in the Larsen C Ice Shelf, Antarctica

Daniel McGrath[1], Konrad Steffen[2,3,4], Paul R. Holland[5], Ted Scambos[6], Harihar Rajaram[7], Waleed Abdalati[1], and Eric Rignot[8,9]

[1]Cooperative Institute for Research in Environmental Sciences, University of Colorado Boulder, Boulder, Colorado, USA, [2]Swiss Federal Institute for Forest, Snow and Landscape Research, Birmensdorf, Switzerland, [3]Swiss Federal Institute of Technology, Zürich, Switzerland, [4]École Polytechnique Federal de Lausanne, Switzerland, [5]British Antarctic Survey, Cambridge, UK, [6]National Snow and Ice Data Center/CIRES, University of Colorado Boulder, Boulder, Colorado, USA, [7]Department of Civil Engineering, University of Colorado Boulder, Boulder, Colorado, USA, [8]Department of Earth System Science, University of California Irvine, Irvine, California, USA, [9]Jet Propulsion Laboratory, California Institute of Technology, Pasadena, California, USA

Abstract Ice shelf fractures frequently terminate where they encounter suture zones, regions of material heterogeneity that form between meteoric inflows in ice shelves. This heterogeneity can consist of marine ice, meteoric ice with modified rheological properties, or the presence of fractures. Here, we use radar observations on the Larsen C Ice Shelf, Antarctica, to investigate (i) the termination of a 25 km long rift in the Churchill Peninsula suture zone, which was found to contain ~60 m of accreted marine ice, and (ii) the along-flow evolution of a suture zone originating at Cole Peninsula. We determine a steady state field of basal melting/freezing rates and apply it to a flowline model to delineate the along-flow evolution of layers within the ice shelf. The thickening surface wedge of locally accumulated meteoric ice, which likely has limited lateral variation in its mechanical properties, accounts for ~60% of the total ice thickness near the calving front. Thus, we infer that the lower ~40% of the ice column and the material heterogeneities present there are responsible for resisting fracture propagation and thereby delaying tabular calving events, as demonstrated in the >40 year time series leading up to the 2004/2005 calving event for Larsen C. This likely represents a highly sensitive aspect of ice shelf stability, as changes in the oceanic forcing may lead to the loss of this heterogeneity.

1. Introduction

1.1. Ice Shelf Structure

Early surveys of the Larsen Ice Shelf by *Mason* [1950] and *Fleet* [1965] described its complex surface, including large-scale rifts and "lenticular holes," later termed dolines. The first comprehensive airborne radar echo soundings of Larsen C helped elucidate the composite nature of the ice shelf, in that a number of glaciers had a "pronounced effect on the ice thickness" [*Smith*, 1972]. It was suggested that the large seaward protrusion in the southeasterly sector of the ice shelf (which subsequently calved off in 1986) might be related to the high flux of grounded meteoric ice from Mobiloil Inlet (Figure 1) [*Smith*, 1972]. Large peninsulas separate these individual inflows and subsequently limit the flux of meteoric ice across the grounding line in these regions, resulting in surface depressions, and hence thickness anomalies, in the ice shelf immediately downstream [*Ridley et al.*, 1989].

The flowbands that originate downstream of peninsulas are typically termed suture zones for their ability to bind together neighboring meteoric inflows and are typically composed of an ice mélange consisting of marine ice, sea ice (formed in open rifts), fallen meteoric blocks, and in situ snowfall [*Glasser et al.*, 2009; *Jansen et al.*, 2013]. In certain cases, where the grounding line transition is smooth and a small catchment area exists on the peninsula, there may be an additional influx of meteoric ice, albeit much less than the major inflows. Suture zone flowbands are frequently compressed laterally by the spreading flow of the thicker meteoric inflows on both sides, resulting in strain thickening of this flowband in the along-flow direction. Suture zones are inconsistent in both appearance and function. First, in terms of appearance, suture zones almost uniformly appear "smooth" in visible imagery despite having a highly variable composition [*Glasser et al.*, 2009; *Holland et al.*, 2009]. This discrepancy is likely due to the fact that suture zones lack large-scale fractures common to meteoric inflows. Further, preferential surface accumulation likely occurs in the surface depressions immediately downstream of the peninsula, acting to homogenize surface variations [*Leonard et al.*, 2008]. Second, in terms of function, large-scale lateral fractures frequently terminate at the edge of suture zones, despite these zones
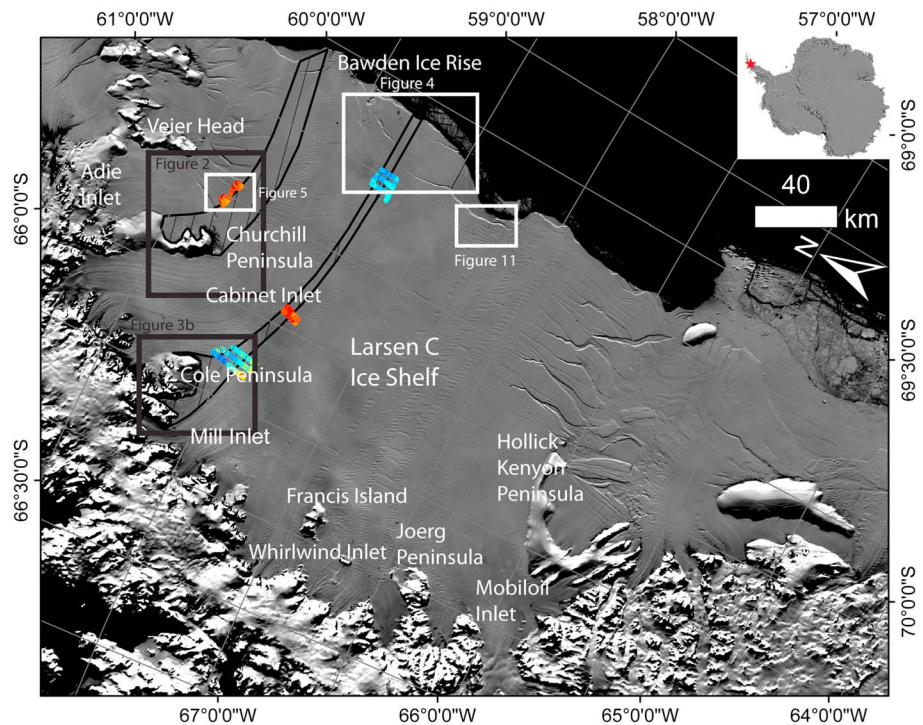
Figure 1. MODIS Mosaic of Antarctica (MOA) [*Haran et al.*, 2005] of the Larsen C Ice Shelf with prominent geographic features labeled. Labeled boxes outline figure locations. Inset: Location of the Larsen C Ice Shelf on the Antarctic Peninsula.

being both thinner and lacking the coherent structure of meteoric inflows, both characteristics potentially indicative of being weak points in an ice shelf. Fracture termination has largely been attributed to the lower inferred stiffness or flow law parameter of suture zones, hence making them "softer" but subsequently also "stronger" than neighboring meteoric ice due to a higher fracture toughness [*Rignot and MacAyeal*, 1998; *Fahnestock et al.*, 2000; *Larour et al.*, 2004; *Bassis et al.*, 2007; *Hulbe et al.*, 2010; *Khazendar et al.*, 2011; *Jansen et al.*, 2013]. The lower stiffness is likely due to variations in material composition, temperature, fabric, presence of impurities, and water content within suture zones [*Cuffey and Paterson*, 2010].

A prominent example of this process on the Larsen C Ice Shelf can be seen in the series of large rifts (~25 km in length) that extend across Adie Inlet and coherently terminate on the suture zone originating from Churchill Peninsula (Figure 2). These rifts and a series of the basal crevasses immediately to the south of the suture zone [*McGrath et al.*, 2012] show no significant change in length between 1963 and present day (Figure 2). Similar behavior is exhibited by the rifts which propagate downstream of the Hollick-Kenyon Peninsula in the southern sector of Larsen C [*Glasser et al.*, 2009]. Importantly, *Hulbe et al.* [2010] demonstrated that if ice shelf fractures did not encounter the lateral heterogeneity of a suture zone, they would continue to propagate and contribute more significantly to future calving events. This result places considerable impetus on further understanding the material composition and along-flow evolution of suture zones, of which there have been few focused studies.

1.2. Formation and Properties of Marine Ice

A key component of suture zone mélange is likely marine ice, which typically forms when plumes of buoyant ice shelf meltwater rise and then supercool due to the reduction in pressure [*de Q. Robin*, 1979]. Beneath Larsen C, a likely source of such meltwater is basal melting of the deep meteoric inflows proximal to the grounding line [*Holland et al.*, 2009], where the thermal forcing is greatest due to the depression of the melting point of ice at elevated pressures. Other possible sources of meltwater occur where rapid tidal currents induce high basal melt rates, often near the calving front and along certain peninsulas/ice rises [*Mueller et al.*, 2012]. The buoyant meltwater plumes that result refreeze to the ice shelf at shallower depths, commonly in ice draft minima found downstream of peninsulas [*Holland et al.*, 2009]. Initially, basally accreted marine ice is likely permeable and slushy in nature but subsequently consolidates due to the accretion of new layers below and through
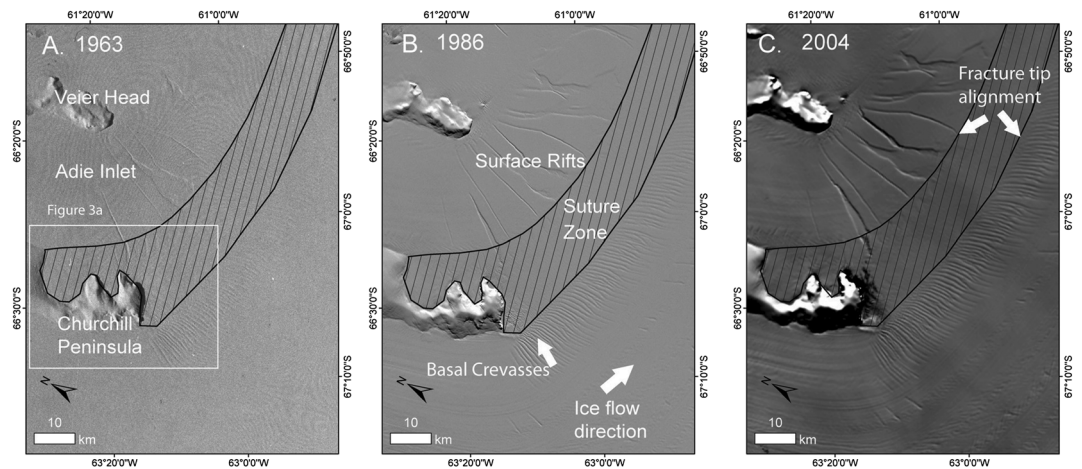
Figure 2. (a) 1963 Declassified Intelligence Satellite Argon Photographic (DISP) image of Adie Inlet [*Kim et al.*, 2007]. (b) 1986 Landsat image of same region showing coherent and stable termination of fractures on suture zone downstream of Churchill Peninsula. (c) 2003/2004 MOA image showing continued stable fracture tip alignment.

conductive heat flux toward the ice shelf surface [*Craven et al.*, 2009; *Hubbard et al.*, 2012]. Marine ice infills thin and potentially weak locations within ice shelves and provides a stabilizing cohesion between neighboring meteoric inputs to the ice shelf [*Glasser et al.*, 2009; *Holland et al.*, 2009].

Two additional processes likely contribute to the formation of marine ice as well, although both likely operate on smaller spatial scales than the previously described process. Basal melting may occur along the sides of individual fractures, which can drive a similar, but more localized convective circulation pattern, resulting in marine ice accretion at shallower depths in the fracture [*Khazendar and Jenkins*, 2003; *Hubbard et al.*, 2012; *Jordan et al.*, 2014]. Marine ice also forms where seawater laterally infiltrates firn prior to pore close-off, a process that likely occurs along rift edges [*Smith and Evans*, 1972; *Hubbard et al.*, 2012].

Thus, potential causes of the modified material properties in suture zones include the presence of (i) marine ice, which tends to be close to the freezing temperature of sea water, hence warmer than the meteoric ice that has been advected from the cold interior, (ii) extensive small fractures, which can act to diffuse the stress intensity at the tip of large-scale laterally propagating fractures, (iii) altered crystal fabric at the lateral edges of the meteoric ice that form the bounds of the suture zones due to past shear, and (iv) impurities. Recent laboratory experiments found that marine ice was consistently more difficult to deform than meteoric ice under the given stress conditions [*Dierckx and Tison*, 2013]. Thus, the lower viscosity of marine ice in regards to rift termination is likely related to the temperature anomaly of marine ice relative to meteoric ice rather than an intrinsic material property [*Dierckx and Tison*, 2013].

In this study, we combine in situ ground penetrating radar surveys, with remote sensing and flowline modeling of two suture zones on the Larsen C Ice Shelf to evaluate the vertical structure, composition and the along-flow evolution of these zones in order to better understand their capacity to terminate large-scale fractures and hence prevent the destabilization of ice shelves.

2. Study Area

Larsen C is the largest ice shelf on the Antarctic Peninsula, consisting of ~50,000 km^2 of floating ice, which is fed from 12 major outlet glaciers flowing off the mountainous spine of the peninsula (Figure 1) [*Cook and Vaughan*, 2010; *Glasser et al.*, 2009]. The ice shelf thickness field is dominated by these major meteoric inflows, which exceed 1000 m at the grounding line and thin to ~200 m by the ice front, with a typical midshelf thickness of 250–400 m [*Griggs and Bamber*, 2009]. Numerous promontories, such as Churchill and Cole Peninsulas, separate these meteoric inflows and extend 20–30 km into the ice shelf domain (Figures 3a and 3b). In some places, the ice-covered sections of the peninsula slope gradually toward the ice shelf, creating a smooth transition from grounded to floating ice (Figure 3c). Elsewhere, the transition is abrupt and the ice shelf surface just downstream is often heavily fractured, although these fractures are not apparently open to
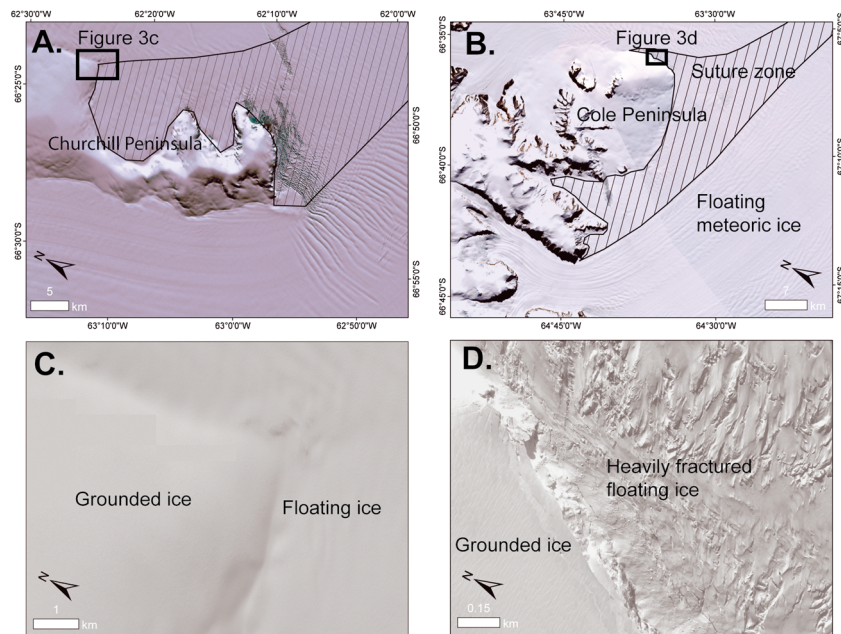
Figure 3. Subset of the Landsat Imagery Mosaic of Antarctica (http://lima.usgs.gov/) detailing the suture zone downstream of (a) Churchill Peninsula and (b) Cole Peninsula. (c) A smooth transition from grounded to floating ice for a section of Churchill Peninsula (Worldview-1 50 cm visible imagery from October 2011). (d) Abrupt transition from grounded ice on Cole Peninsula to heavily fractured floating ice (Worldview-1 50 cm imagery from February 2012). Location of Figures 3c and 3d are indicated by black boxes. Figures 3c and 3d, copyright by Digital Globe, Inc., 2012.

sea level (Figure 3d). The contribution of grounded meteoric ice to the ice mélange likely differs based on the configurations described above, although even in the latter, numerous discrete blocks (~10 m) of meteoric ice have transferred from the grounded region to the ice shelf.

The extent of Larsen C has been relatively stable over the last five decades, with the exception of calving events in 1986 and 2004/2005 where the ice shelf lost ~7700 km^2 and ~1500 km^2, respectively [*Glasser et al.*, 2009; *Cook and Vaughan*, 2010]. The latter calving event occurred after a rift propagated through the suture zone that can be traced downstream from Cole Peninsula (Figure 4). Numerous large (>20 km) rifts, originating at the calving front, were observed to terminate at the approximate lateral edges of this suture zone prior to the 2004–2005 calving event (Figure 4). Despite limited changes in areal extent, the surface elevation of Larsen C has lowered at a rate of between 0.06 ± 0.01 and 0.09 ± 0.01 m a^{-1} during the 1978–2008 period, with the greatest lowering occurring in the northern sector [*Shepherd et al.*, 2003; *Fricker and Padman*, 2012; *Pritchard et al.*, 2012]. This surface lowering is likely dominated by firn densification driven by warmer air temperatures and increased meltwater production/refreezing [*Holland et al.*, 2011; *Fricker and Padman*, 2012; *Pritchard et al.*, 2012] rather than increased basal melting driven by an oceanic forcing [*Shepherd et al.*, 2003; *Nicholls et al.*, 2012]. Oceanographic observations suggest that the primary water mass in the Larsen C cavity is High Salinity Shelf Water (HSSW), which has origins in Modified Weddell Deep Water but has been cooled to the surface freezing point by wintertime sea ice production [*Nicholls et al.*, 2004, 2012]. While HSSW has sufficient thermal forcing to drive weak basal melt, the rates are significantly lower than in ice shelves whose cavities are filled with Circumpolar Deep Water, such as those in the Amundsen Sea Sector [*Pritchard et al.*, 2012]. Further, as HSSW is fixed to the surface freezing point, the only manner by which basal melt rates could increase is through the increased production and flux of HSSW through the cavity, which has not been observed [*Nicholls et al.*, 2012].

3. Radar Survey

3.1. Methods

Radar surveys were conducted with a Malå Geosciences ground based 25 MHz pulse radar system towed behind a snowmobile in November 2011. The radar data were processed by applying a dewow and band-pass filter, custom gain function and corrected for surface topography. The ice shelf-ocean interface
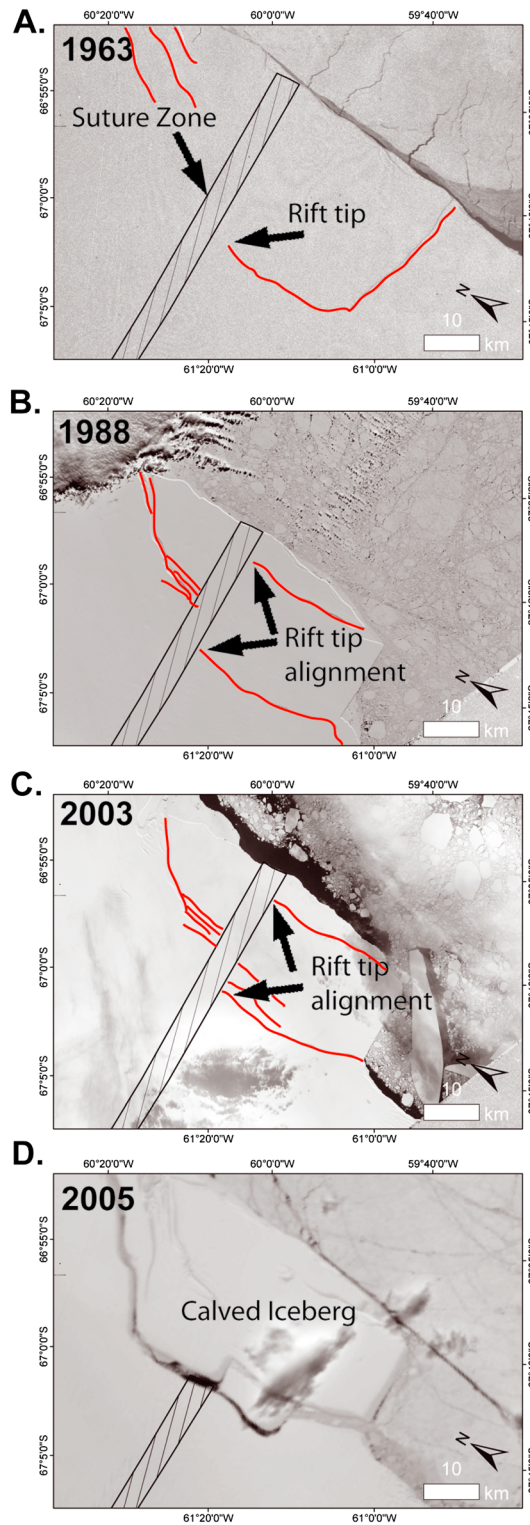
Figure 4. (a) DISP, (b, c) Landsat, and (d) MODIS imagery of Cole Peninsula suture zone (noted by hatching) near calving front (see Figure 1 for figure extent). Laterally propagating rifts show coherent and temporally stable termination along the lateral edges of this zone throughout this period prior to rift penetration and subsequent calving of ~1500 km² iceberg.

reflection was manually delineated along the profiles by following the maximum amplitude in the radar waveform at the appropriate depth. It is important to note that the presence of marine ice can obscure radar returns due to the high dielectric absorption of this material [*Thyssen*, 1988]. Simultaneous position data were collected with a Trimble GeoXH dual-channel GPS, which was postprocessed and corrected to mean sea level using the Eigen GL06C geoid [*Förste et al.*, 2008], tidal amplitude using Circum-Antarctic Tidal Simulation version 2008a (CATS2008a), updated from *Padman et al.* [2002], and a dynamic ocean topography correction of 1.07 m (http://grace.jpl.nasa.gov; *Tapley et al.* [2003]). We estimate the error for the measured surface elevation to be ± 0.5 m. The measured two-way travel time and surface elevation were combined to derive the total ice shelf (ice plus air) thickness following *Holland et al.* [2011]. This method produces spatially variable column-averaged densities, which are subsequently used to derive radar velocities, which range between 0.168 and 0.170 m ns^{-1}. A slight west-to-east positive gradient exists in the calculated radar velocities, which reflects the decrease in surface melt (and hence increase in air content) in this direction [*Holland et al.*, 2011].

In areas with no basal reflector, an "equivalent meteoric ice thickness" (Z) was calculated based on measured surface elevations and the assumption of hydrostatic equilibrium. A local firn air correction, h_{air}, was derived by applying the method of *Holland et al.* [2011] to the areas of the relevant radar profile that do have a clear basal reflector. h_{air} ranges from 4 to 12 m. The ice thickness is then derived from

$$Z = \frac{(z_s - h_{air})\rho_w}{(\rho_w - \rho_i)} + h_{air}, \qquad (1)$$

where z_s is the surface elevation above mean sea level, ρ_w is the density of sea water (1028 kg m^{-3}), and ρ_i is the density of pure ice (917 kg m^{-3}). We estimate the relative error in the calculated ice thickness to be ± 14%, which is the sum in quadrature of the individual errors in surface height (± 0.5 m), pure ice density (± 1 kg m^{-3}), seawater density (± 1 kg m^{-3}), and the firn air correction (± 1.5 m).
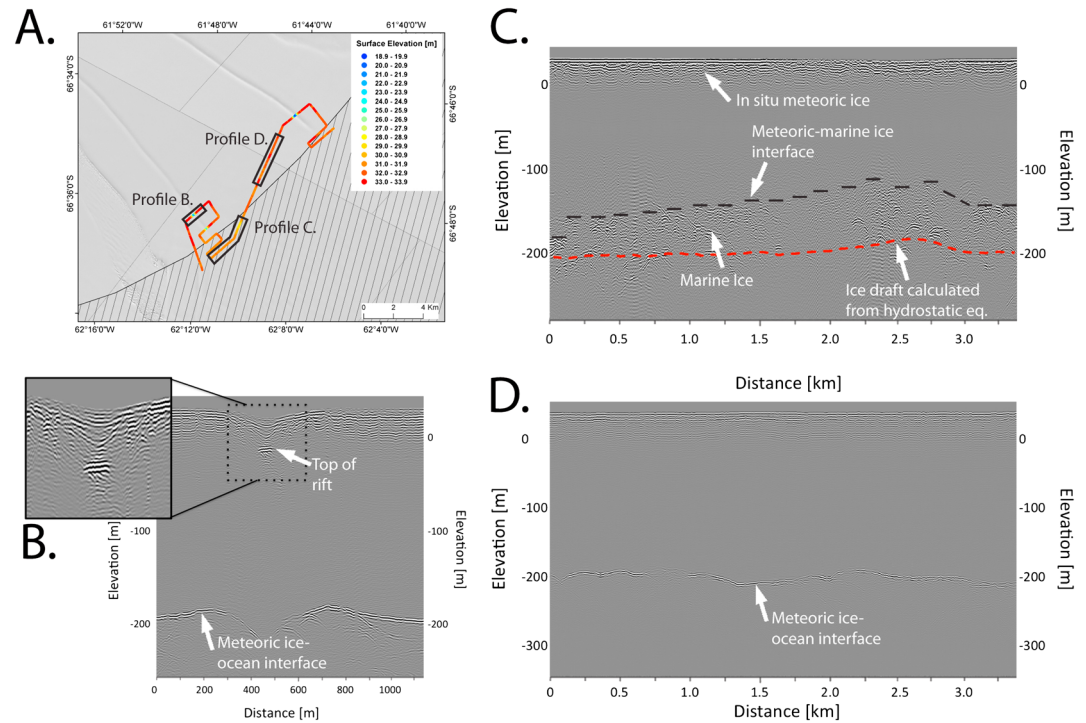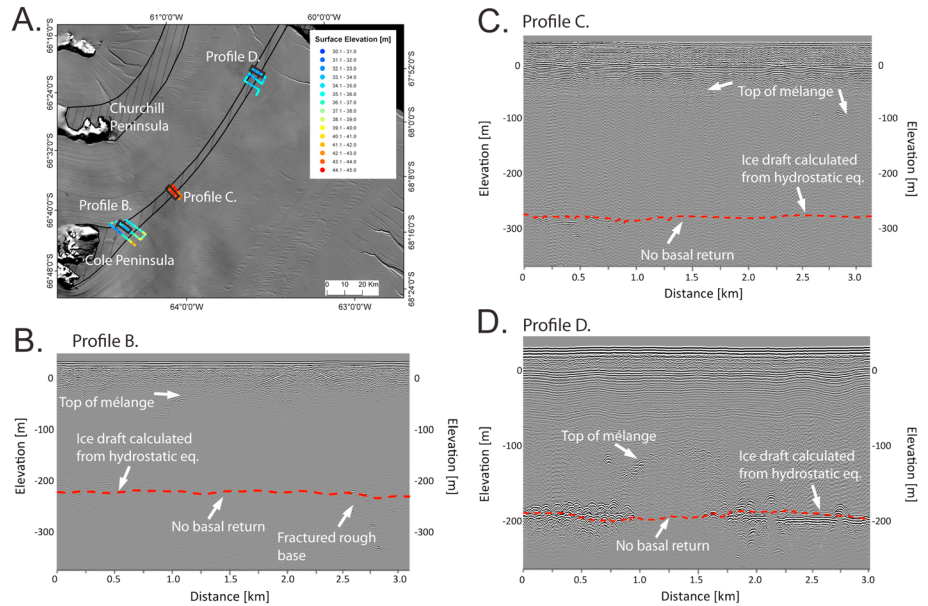
Figure 5. (a) Worldview-1 50 cm visible imagery (October 2011) of Adie Inlet fractures and Churchill Peninsula suture zone. Surface elevations from ground penetrating radar survey are overlaid. (b) Radargram crossing rift. (c) Radargram in suture zone. (d) Radargram showing clear meteoric ice-ocean interface after exiting suture zone flowband. Locations of Figures 5b and 5d are indicated by black boxes. Figure 5a, copyright by Digital Globe, Inc., 2012.

We identify and delineate suture zones as the regions downstream of peninsulas, whose surface appears comparably smooth in visible satellite imagery (Figure 1). The lateral boundaries are defined by tracing surface lineations at the edge of the meteoric inflows to either side and indicated by hatched zones. As outlined, suture zones are relatively wide features encompassing the entire flowband downstream of the peninsulas, while the regions of material heterogeneity are likely narrow, laterally discrete features within these larger flowbands.

3.2. Radar Observations

In situ radar observations were conducted perpendicular to the southern tip of a large rift in Adie Inlet, crossing both the rift tip and the ice immediately to the south of rift termination (Figure 5). The surface expression of the rift is a concave trough, approximately 300 m wide and 10 m deep, which was consistently bridged across the entire width. Radar observations show a strong, smooth basal reflector on either side of the rift, interpreted as the meteoric ice-ocean interface, and a strong, near horizontal reflector aligned with the trough minima and at an approximate depth of 5 m below sea level (Figure 5b). Continuous internal reflectors are observed in the upper 30 m of the radargram and extend across the rift, which is consistent with annual layers of locally accumulated meteoric snow and firn. A second radar transect (Figure 5c), also perpendicular to the rift but ~3 km south (aligned with axis of rift propagation) of the previous transect and 1.25 km beyond the last surface expression of the rift, was conducted in the suture zone (indicated by hatched region in Figure 5a). In contrast to the previous radar transect, weak and mottled reflectors exist over a range of depths, first appearing in the ice column 140–185 m below the surface and extending for another 70–90 m (Figure 5c). The strength of the reflection varies over this thickness, and there is no evidence of a distinct basal interface. A strong, clear basal reflector emerges along the final profile collected outside of the suture zone in the predominantly meteoric Adie Inlet (Figure 5d).

The initial interpretation of the radargram is as follows. In the suture zone, the lack of a strong basal return, and the presence of weak and mottled reflectors, which first emerge at ~140 m below the surface, is consistent with the presence of basally accreted marine ice. The emergence of a strong basal return at the

Figure 6. (a) MOA image of the central Larsen C Ice Shelf and Cole Peninsula suture zone. Surface elevations from ground penetrating radar survey are overlaid. Black hatched regions indicate the Cole and Churchill Peninsula suture zones. Radargrams are shown crossing suture zone at (b) 18 km, (c) 52 km, and (d) 131 km from grounding line. Red dashed line in Figures 6b–6d is ice draft calculated from measured surface elevation and assumptions of hydrostatic equilibrium. The top of the mélange is identified by numerous hyperbolae in the radargrams, indicative of sharp, corner reflectors.

end of the profile is consistent with the transect path, which exits the Churchill Peninsula suture zone and crosses back into the meteoric origin Adie Inlet flowband. If we assume the emergence of the weak internal reflectors corresponds to the meteoric-marine ice interface, then ~60 m of marine ice would exist to the depth of the calculated bottom or ~70–90 m to the deepest of the weak, mottled reflectors.

We also sought to examine the along-flow evolution of suture zone flowbands and thus conducted a series of perpendicular radar transects at progressive distances (18, 52, and 131 km) along the Cole Peninsula suture zone (Figure 6). Cole Peninsula protrudes ~30 km into the ice shelf domain and limits the direct input of meteoric ice, hence creating the ice thickness anomaly immediately downstream (Figure 6a). The meteoric ice inflows through Cabinet and Mill Inlets rapidly compress the suture zone from a width of ~18 km to ~5 km over the first 40 km of its flow path (Figure 6a). Along all profiles, continuous or near-continuous internal reflectors are observed in the upper 40–60 m of the ice column, consistent with annual layers of locally accumulated meteoric snow/firn. In addition, all radargrams exhibit discrete sections in the across-flow direction in which the basal return is obscured by a series of hyperbolae within the ice column. These hyperbolae, which are characteristic of sharp corner reflectors such as crevasses, scatter the radar energy, thereby precluding a return from greater depths. We calculate ice drafts using equation (1) for reference (red dashed lines). Importantly, and in contrast to the Churchill Peninsula radargrams, these reflectors are initially observed 50–90 m below the ice surface (Figure 6b) and then progressively deeper (90 to 150 m and then 130–155 m) in subsequent profiles in the along-flow direction (Figures 6c and 6d).

The initial interpretation is that the hyperbolae observed at progressively greater depths in the ice column in each of the suture zone perpendicular radar profiles originate from the heavily fractured ice mélange present at the surface in the immediate wake of Cole Peninsula (Figure 3d). This interface is observed at progressively greater depths since it is being buried by locally accumulated meteoric ice while flowing toward the calving front. Further, the rough heavily fractured character of the Cole Peninsula radar returns is significantly different from the smooth, mottled returns observed in the suture zone downstream of Churchill Peninsula and previously interpreted as returns from the meteoric-marine ice interface. However, the fractured/rough interface scatters the radar energy and precludes a radar return from greater depths in these discrete sections, and thus, no further information is known about the remainder of the ice column. However, the calculated ice drafts support the presence of ice beneath this layer and thus require continued investigation to characterize its properties.

MCGRATH ET AL.
594
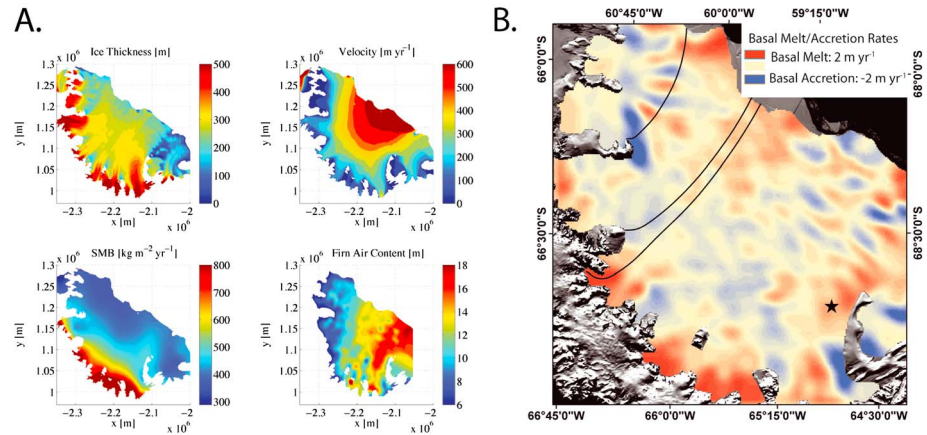
Figure 7. (a) Subpanels of model inputs including ice thickness [*Griggs and Bamber*, 2009], ice velocity [*Rignot et al.*, 2011], surface mass balance [*Lenaerts et al.*, 2012], and firn air content [*Holland et al.*, 2011]. (b) Steady state field of basal melt/accretion rates for the Larsen C Ice Shelf. Basal melting is positive and basal accretion is negative. The flowline cross sections shown in Figure 9 are indicated by black lines. Mass is reported as meters of water equivalent [1000 kg m^{-3}]. Black star indicates location of observed melt rate [*Nicholls et al.*, 2012].

4. Evolution of Ice Shelf Structure

4.1. Basal Melting/Freezing Rates

In order to apply a flowline model to the suture zones studied above, we estimate the basal melting and freezing beneath Larsen C Ice Shelf using a mass flux divergence calculation. Mass conservation can be expressed by

$$\frac{\partial(\rho Z)}{\partial t} + \nabla(\rho \mathbf{V}Z) = \dot{a} - \dot{b}, \tag{2}$$

where Z and ρ are the thickness and mean density of the ice column, respectively, $\mathbf{V}$ is the ice surface velocity vector, $\dot{a}$ is the surface net mass accumulation rate, and $\dot{b}$ is the basal mass melting/freezing rate (positive is melting). We assume that the surface velocity represents the depth average for a floating ice shelf [*Cuffey and Paterson*, 2010].

We proceed by assuming the ice shelf mass is in steady state, $\partial \rho Z / \partial t = 0$, which is justified on the basis that the observed surface lowering is likely due to densification rather than mass removal [*Holland et al.*, 2011; *Fricker and Padman*, 2012; *Pritchard et al.*, 2012]. Even if this interpretation of the recent lowering were incorrect, the rapid modern mass imbalance could not have been operating for a significant fraction of the long (~400 year) advective time scales of the flowline models used below, so the steady state assumption is adequate for our purposes. In steady state, the horizontal divergence of the mass flux is balanced by the sum of both the surface accumulation and basal melting/freezing contribution, and hence is expressed as

$$\dot{b} = \dot{a} - \nabla(\rho \mathbf{V}Z). \tag{3}$$

The data sets used in this analysis include (i) ice thickness and density calculated from surface elevations from satellite radar altimetry [*Griggs and Bamber*, 2009], a derived firn-air grid [*Holland et al.*, 2011], and the assumption of hydrostatic equilibrium; (ii) interferometric synthetic aperture radar (InSAR)-derived ice velocities from the Making Earth System Data Records for Use in Research Environments (MEaSUREs) project [*Rignot et al.*, 2011], and (iii) surface mass balance from the RACMO2.1/Ant model [*Lenaerts et al.*, 2012]. All data sets were compiled to a common reference frame with 1 km grid cells in a polar stereographic projection, allowing us to derive the steady-state basal melting/freezing rates from equation (3) on that grid. We estimate the relative error in basal melting/freezing rates to be ± 20%, which represents the sum in quadrature of the individual relative errors in ice thickness (± 43 m), ice velocity (± 4 m yr^{-1}), surface mass balance (± 67 mm water eq. yr^{-1}), and column-averaged density (± 3 kg m^{-3}).

The nominal resolution of most of the source data is considerably coarser than the 1 km grid, and the method uses spatial derivatives, so the resulting melting/freezing field is noisy, even after smoothing with 9 km filter (Figure 7). For example, the wave-like pattern downstream of Adie Inlet is likely, at least partially, an artifact due to the advection of large rifts, although nonuniform rates would certainly be expected in such regions
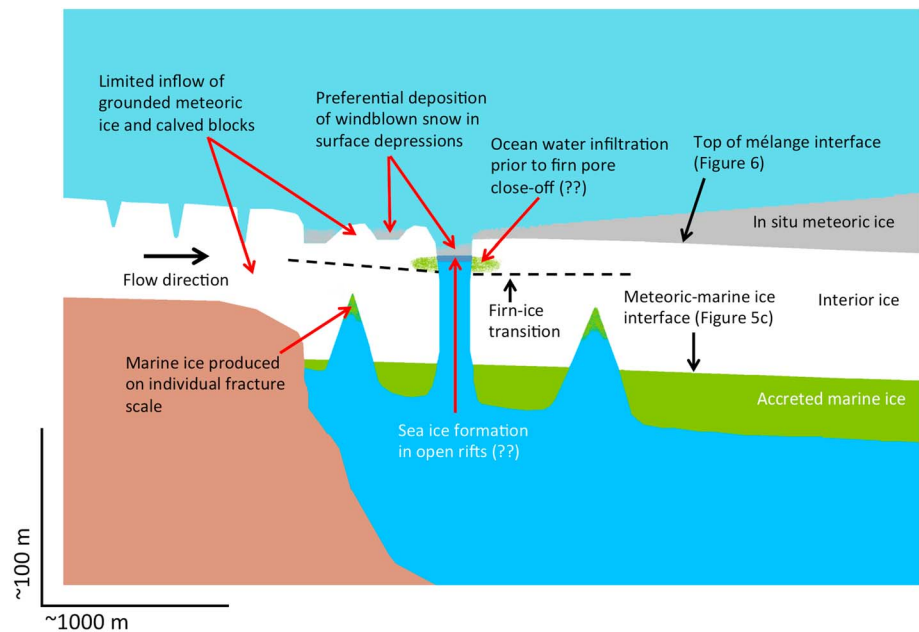
Figure 8. Idealized schematic diagram detailing numerous physical processes that contribute to "interior ice" formed at the origin of suture zones. Interior ice constitutes all ice column thickness that is not attributed to accumulated meteoric ice or basally accreted marine ice in the relatively coarse mass balance calculations. The relative thickness of individual layers is dependent on both process and model uncertainties. Processes marked by (??) indicate high uncertainty in their potential contribution. Radar reflectors shown in Figures 5 and 6 are indicated.

[*Rignot et al.*, 2013]. Highly accurate and temporally coincident ice thickness and velocity fields would be needed to realistically calculate the mass divergence in the presence of these topographic features. Nevertheless, the derived field agrees well with previous studies [*Holland et al.*, 2009; *Mueller et al.*, 2012; *Nicholls et al.*, 2012; *Jansen et al.*, 2013; *Rignot et al.*, 2013]. The method reproduces a modeled pattern of melting beneath deep grounding lines and refreezing in suture zones [*Holland et al.*, 2009], with a particularly vigorous refreezing off Churchill Peninsula that *Holland et al.* [2009] propose to be due to a major confluence of meltwater plumes. In addition, the areas of rapid melting near Bawden Ice Rise and along the Hollick-Kenyon Peninsula agree with predictions of strong tidally driven melting in those areas [*Mueller et al.*, 2012]. Finally, the calculated rate of $0.9 \pm 0.2\,\mathrm{m\,yr^{-1}}$ agrees well with a direct observation (indicated by black star in Figure 7b) of $1.3 \pm 0.2\,\mathrm{m\,yr^{-1}}$ melting in the Hollick-Kenyon Peninsula region [*Nicholls et al.*, 2012]. It is worthwhile to note that an overall reasonable agreement is achieved despite the independent methods (mass flux divergence, in situ observations, ocean models) used to derive these estimates.

4.2. Along-flow Evolution

We now consider the evolution of ice structure along flowlines originating at the grounding lines of both Cole and Churchill Peninsula, and Mill Inlet (black flowlines in Figure 7). The ice is conceived to be comprised of three layers: a surface "locally accumulated meteoric ice" layer built up by mean surface mass balance rates from the RACMO2.1/Ant model [*Lenaerts et al.*, 2012], a "basally accreted marine ice" layer according to the basal melting/freezing field described above, and an "interior ice" layer occupying the remainder of the ice column, not prescribed to either of the two previous layers.

There are numerous physical processes that likely contribute to the presence of interior ice (Figure 8). First, to some extent, interior ice consists of the previously discussed ice mélange observed in the immediate wake of these peninsulas, of which marine ice is an important component. However, many of these processes operate on a spatial scale insufficient to be resolved by the large-scale mass conservation model (Figure 8). Thus, we make the distinction between large-scale "basally-accreted marine ice" and marine ice that forms on the scale of individual rifts and subsequently contributes to interior ice [*Khazendar and Jenkins*, 2003; *Jordan et al.*, 2014]. Second, although peninsulas certainly limit the flux of grounded ice into suture zone flowbands (i.e., no major outlet glaciers), there remain significant regions where slow moving grounded meteoric ice flows into the shelf,

A. Churchill Peninsula

B. Cole Peninsula
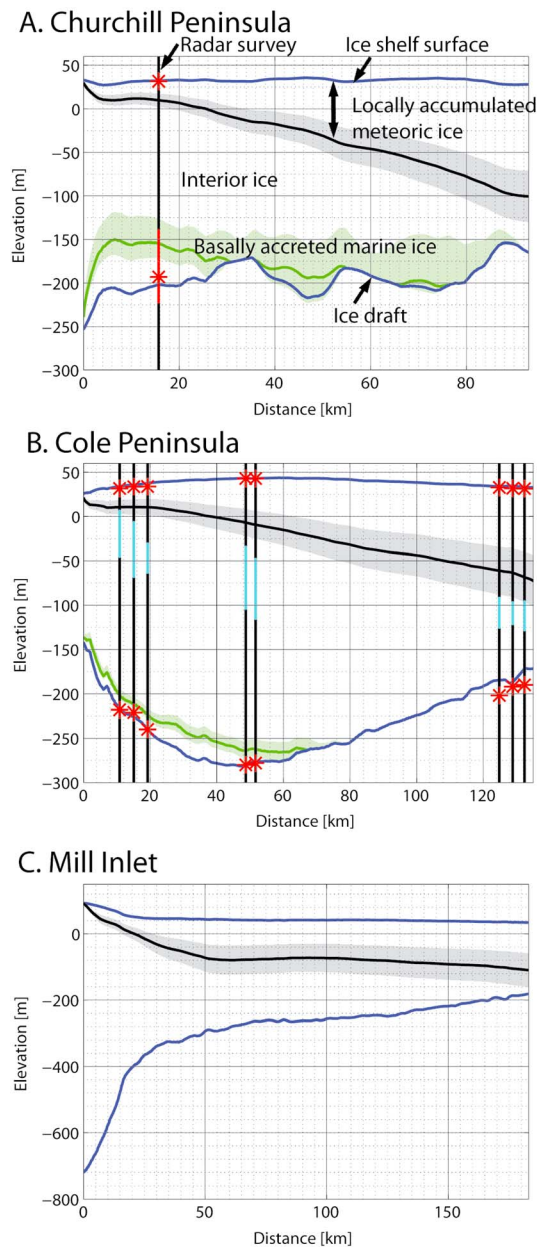
C. Mill Inlet

Figure 9. Flowline cross sections of the Larsen C Ice Shelf along (a) Churchill Peninsula, (b) Cole Peninsula, and (c) Mill Inlet. Surface elevation (blue), ice draft (blue), and interfaces between locally accumulated meteoric ice and interior ice (black) and basally accreted marine ice (green) are shown. The shaded bounds represent the cumulative sensitivity of the model to parameters as discussed in the text. Thin vertical black lines correspond to radar transects, while overlaid red/cyan vertical lines indicate depths of features discussed in the text (section 3.2) and shown in Figures 5 and 6. Red stars are measured surface elevations and either observed/calculated drafts. Note different elevation and distance scales.

as observed for sectors of both Churchill and Cole Peninsulas (Figure 3). This flux is likely not fully accounted for in velocity and thickness fields used as model inputs but nonetheless is likely an important component of the shelf thickness. Therefore, modeled thickness of this layer is dependent on model uncertainties. For example, if the errors were such that the ice thickness gradient were greater or ice velocity slower in reality than in the model inputs, higher basal accretion rates would result, thus creating a thicker basally accreted marine ice layer and less interior ice. Similarly, in comparison to the RACMO2.1/ANT model, higher localized surface accumulation rates likely exist in the wake of peninsulas due to wind redeposition in surface depressions [*Leonard et al.*, 2008]. This would result in a greater thickness of locally accumulated meteoric ice in these zones and a reduced interior ice thickness. Thus, there are clear physical bases to support the presence of interior ice, although the thickness of this layer is dependent on uncertainties in how well model input fields depict reality.

Instantaneous mass flux rates are first converted to cumulative mass by multiplying by the time increment needed for the ice to advect between nodes with 200 m spacing. We convert surface accumulation mass to thickness by applying an offset proportional to the firn air volume over this ice thickness [*Holland et al.*, 2011]. We convert marine ice mass to thickness assuming an average bulk density of 935 kg m^{-3}, a value higher than meteoric ice due to the presence of seawater in the permeable lower layers of the marine ice [*Craven et al.*, 2009]. This cumulative thickness at each node is added to the cumulative thickness of the surface and basal layers that exist on the upstream edge of each node.

To apply this technique to the flowline cross section, it is necessary to account for strain thinning. As the surface velocity can normally be assumed to be constant with depth in the bulk of floating ice shelves, we can assume that each of the layers undergoes the same rate of thinning per unit depth. The vertical strain rate ($\dot{\varepsilon}_z$) is related to strain in along-flow and across-flow directions and can be calculated as

$$\dot{\varepsilon}_z = -\left(\dot{\varepsilon}_x + \dot{\varepsilon}_y\right), \qquad (4)$$

where $\dot{\varepsilon}_x$ is the along-flow strain rate and $\dot{\varepsilon}_y$ is the across-flow strain rate. Strain rates are calculated from the InSAR surface velocities [*Rignot et al.*, 2011]. Applying the formulation of *Craven et al.* [2009], we calculate the thickness of both the surface accumulation and basally accreted marine ice layer at the downstream edge of the node (Z_2) compared to its thickness at the upstream edge (Z_1) as

$$Z_2 = Z_1 * e^{\dot{\varepsilon}_z \cdot t} + \frac{\dot{a}}{\dot{\varepsilon}_z}\left(e^{\dot{\varepsilon}_z \cdot t} - 1\right), \tag{5}$$

where t is the time taken to advect between nodes and $\dot{a}$ is representative of the instantaneous rate of mass flux, either at the surface or base of the ice shelf. The resulting surface and basal thicknesses are subsequently superimposed on the ice thickness profile, with the difference between these layers attributed to interior ice [*Griggs and Bamber*, 2009].

We assess the sensitivity of the flowline model to a range of key parameters, including surface velocity (manifested as time to advect between nodes), the vertical strain rate, and both surface and basal melting/freezing rates. The shaded bounds (Figure 9) represent the cumulative sensitivity of the locally accumulated meteoric ice and basally accreted marine ice layers to ± 20% surface velocity, ± 20% vertical strain rate, and ± 20% for surface/basal mass flux rates.

The flowline cross sections shown in Figure 9 delineate the along-flow evolution of the internal structure of the Larsen C Ice Shelf. Surface accumulation forms the upper wedge of the ice shelf and comes to constitute 68 ± 16%, 49 ± 14%, and 64 ± 24% of the total thickness near the calving front along the Churchill, Cole, and Mill flowlines, respectively (Figure 9). Basally accreted marine ice is present along both the Churchill and Cole Peninsulas but not along the meteoric inflow dominated Mill Inlet, which instead experiences high basal melt rates and subsequent thinning. Importantly, the basally accreted marine ice layers, which reach maximum thicknesses of 56 ± 25 and 26 ± 9 m for Churchill and Cole, respectively, are subsequently melted away and do not persist to the calving front along either profile (Figure 9). However, it is important to emphasize that these layers only represent "basal" marine ice accretion, which occurs on a scale large enough to affect the coarse ice thickness and velocity fields. They do not represent the small-scale processes discussed previously, such as the local production of marine ice in rifts or flooding of firn, which is instead therefore allocated to interior ice (Figure 8).

Along the Churchill Peninsula flowline, there is a close agreement between the depth of the meteoric-marine ice interface, as interpreted from the radar observations (Figure 5) and the flowline model (Figure 9a). This agreement supports the initial radar interpretation that these internal reflectors, which first emerge at a depth of 140 m below the surface, represent the meteoric-marine ice interface and that subsequent reflectors below likely originate from within the marine ice.

Along the Cole Peninsula flowline, the close agreement (RMS difference of 29 m) between the depth of the radar returns (distance between shelf surface and red vertical lines in Figure 9b) and the modeled accumulation thickness (distance between shelf surface and black dipping line) gives confidence to our initial interpretation that these reflectors originate from the progressively buried ice mélange that initially forms at the surface immediately downstream of Cole Peninsula. Importantly, and in contrast to Churchill Peninsula, this interface is very clearly not from large-scale basally accreted marine ice. We note, however, a consistent offset of ~30 m between these layers, such that the modeled accumulation accounts for less of the ice column than the radargrams would suggest (Figure 9b). As noted previously, one plausible explanation for this offset is the preferential, above-average accumulation that occurs in surface depressions due to wind redeposition [*Leonard et al.*, 2008] but is not fully represented in the RACMO2.1/Ant model (Figure 8). A second explanation could be that the modeled 1979–2011 mean surface mass balance values underestimate the ~400 year mean values integrated along this flowline, which is consistent with the notion that increased atmospheric flow over the Antarctic Peninsula, associated with the positive polarity of the Southern Annular Mode index, has led to drier, warmer air over Larsen Ice Shelf during recent decades [*Marshall et al.*, 2006]. Another entirely plausible explanation for this offset could be that the source of the radar return originates from sea level at the grounding line rather than from the ice shelf surface, since this would uniformly lower the interface by 25–30 m. A sea level origin would be appropriate if the return were from firn that had been flooded with seawater or from sea ice and marine ice formed in open rifts (Figure 8).
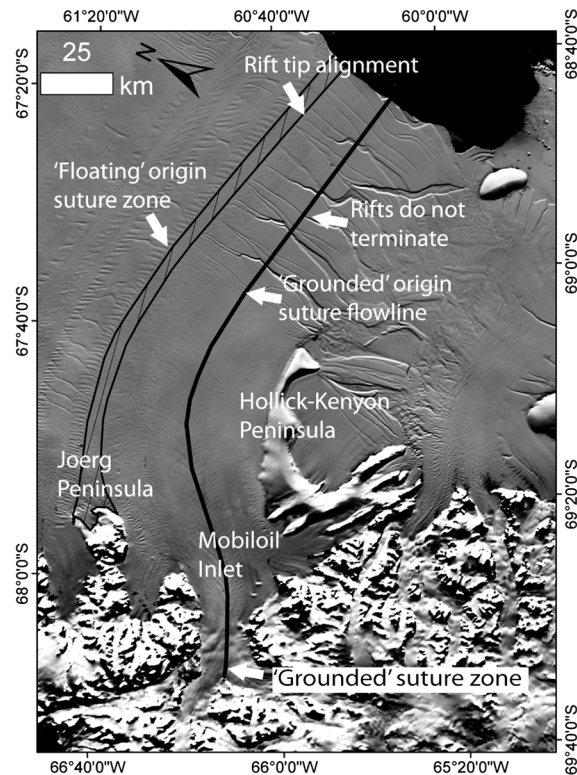
Figure 10. MOA image of the southern sector of the Larsen C Ice Shelf detailing the suture zone that forms in the wake of Joerg Peninsula, which contains marine ice, and the suture zone that forms in a grounded section of Mobiloil Inlet, which does not contain marine ice. Rifts, propagating off the tip of the Hollick-Kenyon Peninsula, extend through the suture zone with grounded origins but coherently terminate along the lateral edge of the Joerg Peninsula suture zone.

5. Discussion

We find direct field and modeling evidence that large-scale rifts in Adie Inlet initially terminate at the lateral edge of the Churchill Peninsula suture zone at a point where >45 m of accreted marine ice exists. While these observations do not determine the mechanism by which the rifts terminate nor the unique material properties responsible for this process, the alignment of these observations offers further confirmation of the importance of marine ice [Glasser et al., 2009; Holland et al., 2009]. Similar to what has been noted for the Hollick-Kenyon rifts in the southern sector of the ice shelf [Glasser et al., 2009; Jansen et al., 2010], these fractures remain bound by the lateral edge of the suture zone all the way to the calving front. Thus, while the initial termination is likely due to the presence of marine ice, it is unclear if the static behavior is simply due to spatial variation in the stress environment (i.e., rifts are opened due to tension next to the peninsulas and bound by the marine ice there, but as they are advected, downstream the tension relaxes so that they do not subsequently propagate regardless of any change in the suture-zone ice structure). Alternatively, this behavior may offer confirmation that some property of the suture zone ice remains sufficiently different to counteract any tension further downstream.

The integrated field and modeling results presented here provide some context by which to evaluate the along-flow evolution of the ice shelf structure and its impact on rift behavior. In all three profiles examined, the wedge of the locally accumulated meteoric ice accounts for ~50–60% of the total ice thickness near the calving front. As this ice has accumulated on the ice shelf surface, it is unlikely that large lateral variations exist in the mechanical properties, regardless of where it accumulated on the ice shelf surface (i.e., a suture zone or meteoric inflow). Thus, there is no reason to suspect that this section of the ice column would exert a strong control on rift behavior. The remaining ~40% of the ice column consists of interior ice, a term that broadly encompasses the ice mélange that forms in the wake of peninsulas rather than "basally accreted" marine ice [Hubbard et al., 2012]. Marine ice originating in rifts and crevasses likely forms an important aspect of this mélange, but direct observations in the form of ice cores are necessary to confirm this point.

The satellite image time series leading up to and just after the 2004/2005 calving event for Larsen C (Figure 4) offers evidence that regardless of whether this section of the ice column contains marine ice, it still has the ability to arrest rift propagation. In the 1963 image, three distinct rifts are seen propagating south toward the suture zone, while a front parallel rift is propagating northward. In all cases, these rifts are present in ice of meteoric origin, comparable to the flowline model for Mill Inlet (Figure 9c). In both the 1988 and 2003 images, numerous rifts are observed to have terminated and stabilized at the approximate lateral edges of the suture zone. The subsequent image (Figure 4d) on 8 January 2005 clearly shows a detached iceberg, the result of the northward propagating rift eventually penetrating through the suture zone. We suggest that the delay in this final propagation was likely due to material heterogeneity present in the lower 40% of the ice column and
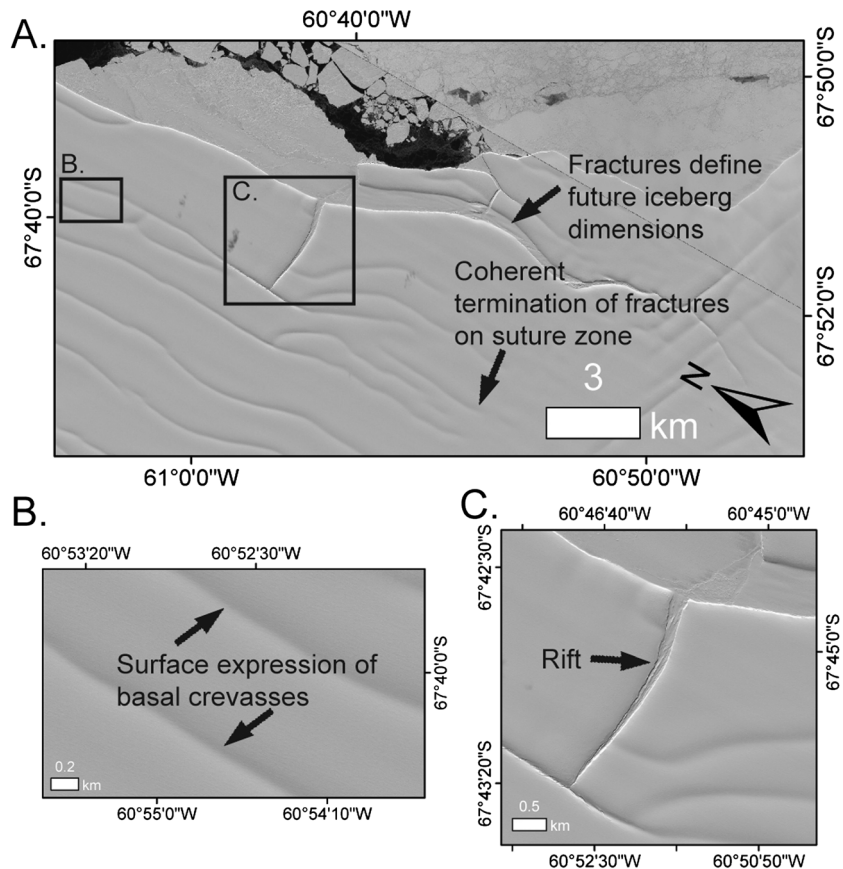
Figure 11. (a) GeoEye-1 50 cm visible imagery (November 2009) of the calving front in the region of ice originating in Whirlwind Inlet, which contains (b) numerous basal crevasses, as indicated by the surface troughs, and (c) an ice mélange filled full thickness rift. Copyright by GeoEye Inc., 2011.

that external forcings that modify or remove this heterogeneity would remove what is likely an important safeguard against the continued propagation of fractures.

One line of anecdotal evidence that supports the notion that marine ice is likely key to the rift termination process can be seen in the southern sector of Larsen C (Figure 10). Two large tributaries of Mobiloil Inlet join together ~10 km upstream of the grounding line, creating a distinct surface lineation that can be traced in the along-flow direction on the floating ice shelf (Figure 10). The series of large rifts/fractures that propagate northward from the eastern tip of the Hollick-Kenyon Peninsula are clearly observed to propagate through this suture zone with grounded origins. These rifts, however, coherently terminate along a second suture zone, which formed in the floating ice shelf domain and is known to contain marine ice [*Holland et al.*, 2009; *Jansen et al.*, 2013]. It is also unknown whether marine ice persists to the calving front here. This observation, while not conclusive, emphasizes that marine ice is likely the key element responsible for rift termination rather than some mechanical properties inherent to all suture zones.

Our observations show discrete zones of heterogeneity, which potentially contain marine ice, to persist to the calving front. This highlights the disproportionally large impact that a small component of the ice thickness can have upon rift propagation and, subsequently, the structural stability of ice shelves. In the absence of the heterogeneity in these zones, the continued propagation of fractures would result in a further weakened ice shelf and likely contribute to increased tabular iceberg calving. Ultimately, this increased calving could threaten the stability of the ice shelf. For example, if the large fractures/rifts that currently terminate in the Churchill and Joerg suture zones were allowed to propagate toward each other, the eastward half of Larsen C, unconstrained by sidewalls, would appear unviable (Figure 1). This is an important, and nonlinear, sensitivity of ice shelves to oceanic forcings, for if either the rate of basal accretion decreases or basal melt increases, such features, located at the base of the ice shelf, would likely be removed.

This sensitivity is further exacerbated because a significant proportion of the fractures on the Larsen C Ice Shelf are initially basal crevasses, rather than full-thickness rifts, and therefore only penetrate through 30–60% of the ice thickness (Figure 11) [*Luckman et al.*, 2012; *McGrath et al.*, 2012]. Thus, the material properties over this lower half of the ice shelf likely exert the greatest control on the behavior of these abundant fractures. The series of fractures near the calving front of Whirlwind Inlet flowband (Figure 1), which are bound on either side by suture zones, appear as broad surface troughs in visible imagery, consistent with their interpretation as basal crevasses (Figure 11b). For comparison, a crosscutting, front-perpendicular rift (with considerable mélange infill) is also shown, which is a notably sharper feature and represents a structural discontinuity within the shelf (Figure 11c). The abundance and likely sensitivity of basal crevasses to the material properties in the lower 50% of the ice column further highlights the important control that these discrete sections of material heterogeneity exert over fracture extent and subsequently to ice shelf stability.

6. Conclusions

In situ radar observations and visible imagery are used to demonstrate that material heterogeneity limits rift propagation in the Larsen C Ice Shelf. Our integrated results confirm ~60 m of marine ice is present where a large 25 km long rift terminates at the Churchill Peninsula suture zone. The along-flow evolution of the suture zone downstream of Cole Peninsula demonstrates that the growing wedge of in situ accumulation, with likely homogenous material properties, comes to account for ~60% of the total ice thickness. The implications of this are twofold: (i) the remaining heterogeneity is sufficient, even as a minority of the total thickness, to arrest rift propagation, and (ii) this represents an important sensitivity of ice shelves, as changes in ocean forcings may modify these features. Changes that contribute to the formation or persistence of this heterogeneity would likely increase the stability of ice shelves, and conversely, changes that erode these features would likely allow fractures to propagate earlier and further, therefore likely increasing tabular iceberg calving rates and ultimately determining the stability of the ice shelf.

References

Bassis, J. N., H. A. Fricker, R. Coleman, Y. Bock, J. Behrens, D. Darnell, M. Okal, and J.-B. Minster (2007), Seismicity and deformation associated with ice-shelf rift propagation, *J. Glaciol.*, *53*(183), 523–536.

Cook, A. J., and D. G. Vaughan (2010), Overview of areal changes of the ice shelves on the Antarctic Peninsula over the past 50 years, *Cryosphere*, *4*, 77–98.

Craven, M., I. Allison, H. A. Fricker, and R. Warner (2009), Properties of a marine ice layer under the Amery Ice Shelf, East Antarctica, *J. Glaciol.*, *55*(192), 717–728.

Cuffey, K. M., and W. S. B. Paterson (2010), *The Physics of Glaciers*, 4th ed., 693 pp., Oxford, Butterworth-Heinemann.

de Q Robin, G. (1979), Formation, flow and disintegration of ice shelves, *J. Glaciol.*, *24*(90), 259–271.

Dierckx, M., and J.-L. Tison (2013), Marine ice deformation experiments: An emperical validation of creep parameters, *Geophys. Res. Lett.*, *40*, 134–138, doi:10.1029/2012GL054197.

Fahnestock, M. A., T. A. Scambos, R. A. Bindschadler, and G. Kvaran (2000), A millennium of variable ice flow recorded by the Ross Ice Shelf, Antarctica, *J. Glaciol.*, *46*(155), 652–664.

Fleet, M. (1965), The occurrence of rifts in the Larsen Ice Shelf near Cape Disappointment, *Br. Antarct. Surv. Bull.*, *6*, 63–66.

Förste, C., et al. (2008), The GeoForschungsZentrum Potsdam/Groupe de Recherche de Geodesie Spatiale satellite-only and combined gravity field models: EIGEN-GL04S1 and EIGEN-GL04C, *J. Geod.*, *82*, 331–346, doi:10.1007/s00190-007-0183-8.

Fricker, H. A., and L. Padman (2012), Thirty years of elevation change on Antarctic Peninsula ice shelves from mulitmission satellite radar altimetry, *J. Geophys. Res.*, *117*, C02026, doi:10.1029/2011JC007126.

Glasser, N. F., B. Kulessa, A. Luckman, D. Jansen, E. C. King, P. R. Sammonds, T. A. Scambos, and K. C. Jezek (2009), Surface structure and stability of the Larsen C ice shelf, Antarctic Peninsula, *J. Glaciol.*, *55*(191), 400–410.

Griggs, J. A., and J. L. Bamber (2009), Ice shelf thickness over Larsen C, Antarctica, derived from satellite altimetry, *Geophys. Res. Lett.*, *36*, L19501, doi:10.1029/2009GL039527.

Haran, T., J. Bohlander, T. Scambos, T. Painter, and M. Fahnestock (2005), updated 2006, *MODIS Mosaic of Antarctica (MOA) Image Map*, National Snow and Ice Data Center, Boulder, Colorado USA, doi:10.7265/N5ZK5DM5.

Holland, P. R., H. F. J. Corr, D. G. Vaughan, A. Jenkins, and P. Skvarca (2009), Marine ice in Larsen Ice Shelf, *Geophys. Res. Lett.*, *36*, L11604, doi:10.1029/2009gl038162.

Holland, P. R., H. F. J. Corr, H. D. Pritchard, D. G. Vaughan, R. J. Arthern, A. Jenkins, and M. Tedesco (2011), The air content of Larsen Ice Shelf, *Geophys. Res. Lett.*, *38*, L10503, doi:10.1029/2011GL047245.

Hubbard, B., J.-L. Tison, F. Pattyn, M. Dierckx, T. Boereboom, and D. Samyn (2012), Optical-televiewer-based identification and characterization of material facies associated with an Antarctic ice-shelf rift, *Ann. Glaciol.*, *53*(60), 137–146, doi:10.3189/2012AoG60A045.

Hulbe, C. L., C. LeDoux, and K. Cruikshank (2010), Propagation of long fractures in the Ronne Ice Shelf, Antarctica, investigated using a numerical model of fracture propagation, *J. Glaciol.*, *56*(197), 459–472.

Jansen, D., B. Kulessa, P. R. Sammonds, A. Luckman, E. C. King, and N. F. Glasser (2010), Present stability of the Larsen C ice shelf, Antarctic Peninsula, *J. Glaciol.*, *56*(198), 593–600.

Jansen, D., A. Luckman, B. Kulessa, P. R. Holland, and E. C. King (2013), Marine ice formation in a suture zone on the Larsen C Ice Shelf and its influence on ice shelf dynamics, *J. Geophys. Res. Earth Surface*, *118*, 1628–1640, doi:10.1002/jgrf.20120.

Jordan, J. R., P. R. Holland, A. Jenkins, M. D. Piggott, and S. Kimura (2014), Modelling ice-ocean interaction in ice shelf crevasses, *J. Geophys. Res. Earth Surface*, doi:10.1002/2013JC009208, in press.

Khazendar, A., and A. Jenkins (2003), A model of marine ice formation within Antarctic ice shelf rifts, *J. Geophys. Res.*, *108*(C73235), doi:10.1029/2002JC001673.

Khazendar, A., E. Rignot, and E. Larour (2011), Acceleration and spatial rheology of Larsen C Ice Shelf, Antarctic Peninsula, *Geophys. Res. Lett.*, *38*, L09502, doi:10.1029/2011GL046775.

Kim, K., K. C. Jezek, and H. Liu (2007), Orthorectified image mosaic of Antarctica from 1963 Argon satellite photography: Image processing and glaciological applications, *Intern. J. Remote Sens.*, *28*(23), 5357–5373.

Larour, E., E. Rignot, and D. Aubry (2004), Modelling of rift propagation on Ronne Ice Shelf, Antarctica, and sensitivity to climate change, *Geophys. Res. Lett.*, *31*, L16404, doi:10.1029/2004GL020077.

Lenaerts, J. T. M., M. R. van den Broeke, W. J. van de Berg, E. van Meijgaar, and P. Kuipers Munneke (2012), A new, high-resolution surface mass balance map of Antarctica (1979–2010) based on regional atmospheric climate modeling, *Geophys. Res. Lett.*, *39*, L04501, doi:10.1029/2011GL050713.

Leonard, K. C., L.-B. Tremblay, D. R. MacAyeal, and S. S. Jacobs (2008), Interactions of wind-transported snow with a rift in the Ross Ice Shelf, Antarctica, *Geophys. Res. Lett.*, *35*, L05501, doi:10.1029/2007GL033005.

Luckman, A., D. Jansen, B. Kulessa, E. C. King, P. Sammonds, and D. I. Benn (2012), Basal crevasses in Larsen C Ice Shelf and implications for their global abundance, *Cryosphere*, *6*, 113–123.

Marshall, G. J., A. Orr, N. P. M. van Lipzig, and J. C. King (2006), The impact of changing Southern Hemisphere Annular Mode on Antarctic Peninsula summer temperatures, *J. Clim.*, *19*, 5388–5404.

Mason, D. (1950), The Larsen Shelf Ice, *J. Glaciol.*, *1*(8), 409–413.

McGrath, D., K. Steffen, T. Scambos, H. Rajaram, G. Casassa, and J. L. Rodriguez Lagos (2012), Basal crevasses and associated surface crevassing on the Larsen C ice shelf, Antarctica, and their role in ice-shelf stability, *Ann. Glaciol.*, *58*(60), 10–18, doi:10.3189/2012AoG60A005.

Mueller, R. D., L. Padman, M. S. Dinniman, S. Y. Erofeeva, H. A. Fricker, and M. A. King (2012), Impact of tide-topography interactions on basal melting of Larsen C Ice Shelf, Antarctica, *J. Geophys. Res.*, *117*, C05005, doi:10.1029/2011JC007263.

Nicholls, K. W., C. J. Pudsey, and P. Morris (2004), Summertime water masses off the northern Larsen C Ice Shelf, Antarctica, *Geophys. Res. Lett.*, *31*, L09309, doi:10.1029/2004GL019924.

Nicholls, K. W., K. Makinson, and E. J. Venables (2012), Ocean circulation beneath Larsen C Ice Shelf, Antarctica from in situ observations, *Geophys. Res. Lett.*, *39*, L19608, doi:10.1029/2012GL053187.

Padman, L., H. A. Fricker, R. Coleman, S. Howard, and L. Erofeeva (2002), A new tide model for the Antarctic ice shelves and seas, *Ann. Glaciol.*, *34*, 247–254.

Pritchard, H. D., S. R. M. Lichtenberg, H. A. Fricker, D. G. Vaughan, M. R. van den Broeke, and L. Padman (2012), Antarctic ice-sheet loss driven by basal melting of ice shelves, *Nature*, *484*, 502–505, doi:10.1038/nature10968.

Ridley, J., W. Cudlip, N. McIntyre, and C. Rapley (1989), The topography and surface characteristics of the Larsen Ice Shelf, Antarctica, using satellite altimetry, *J. Glaciol.*, *35*(121), 299–310.

Rignot, E., and D. R. MacAyeal (1998), Ice-shelf dynamics near the front of the Filchner-Ronne Ice Shelf, Antarctica, reveal by SAR interferometry, *J. Glaciol.*, *44*(147), 405–418.

Rignot, E., J. Mouginot, and B. Scheuchl (2011), Ice flow of the Antarctic Ice Sheet, *Science*, *333*(1427), doi:10.1126/science.1208336.

Rignot, E., S. Jacobs, J. Mouginot, and B. Scheuchl (2013), Ice-shelf melting around Antarctica, *Science*, *341*(6143), 266–270, doi:10.1126/science.1235798.

Shepherd, A., D. Wingham, T. Payne, and P. Skvarca (2003), Larsen Ice Shelf has progressively thinned, *Science*, *302*(5646), 856–859, doi:10.1126/science.1089768.

Smith, B. M. E. (1972), Airborne radio echo sounding of glaciers in the Antarctic Peninsula, British Antarctic Survey Scientific Reports, 72, 1–11.

Smith, B. M. E., and S. Evans (1972), Radio echo sounding: Absorption and scattering by water inclusion and ice lenses, *J. Glaciol.*, *11*(61), 133–146.

Tapley, B. D., D. P. Chambers, S. Bettadpur, and J. C. Ries (2003), Large scale ocean circulation from the GRACE GGM01 Geoid, *Geophys. Res. Lett.*, *30*(22), doi:10.1029/2003GL018622.

Thyssen, F. (1988), Special aspects of the central part of Filchner-Ronne Ice Shelf, Antarctica, *Ann. Glaciol.*, *11*, 173–179.